RSC Advances

PAPER

View Article Online
View Journal | View Issue

Check for updates

Cite this: *RSC Adv.*, 2019, **9**, 9244

Enhanced photoluminescence and energy transfer performance of $Y_3Al_4GaO_{12}:Mn^{4+},Dy^{3+}$ phosphors for plant growth LED lights†

Mao Xia, ‡[abc] Simin Gu, ‡[ac] Cheng Zhou,[a] Longhai Liu,[a] Yuan Zhong,[ac] Yongli Zhang[ac] and Zhi Zhou*[ac]

Received 26th January 2019
Accepted 12th March 2019

DOI: 10.1039/c9ra00700h

rsc.li/rsc-advances

Plant growth LEDs have attracted broad attention in modern society, desperate for specific phosphors with a characteristic emission band. A novel Mn^{4+} and Dy^{3+} co-doped $Y_3Al_4GaO_{12}$ phosphor were successfully prepared through a conventional high-temperature solid-state reaction. A three band emission including red (625–700 nm), orange (550–607 nm) and blue (462–490 nm) is observed in these phosphors when excited under a near-UV lamp, which is ascribed to $^2E \rightarrow {}^4A_2$ of Mn^{4+}, $^4F_{9/2} \rightarrow {}^6H_{15/2}$ and $^4F_{9/2} \rightarrow {}^6H_{13/2}$ of Dy^{3+}, respectively. The three emissions match the absorption spectra of chlorophyll A and chlorophyll B well. Meanwhile, the energy transfer from Dy^{3+} to Mn^{4+} was confirmed by the luminescence spectra and lifetime analysis. Finally, an LED device was fabricated that consisted of a 365 nm ultraviolet chip and the $Y_3Al_4GaO_{12}:Mn^{4+},Dy^{3+}$ phosphor. The excellent properties indicate that the synthesized phosphor has a promising application in the optical agricultural industry.

Open Access Article. Published on 21 March 2019. Downloaded on 7/13/2025 5:45:08 PM.
This article is licensed under a Creative Commons Attribution-NonCommercial 3.0 Unported Licence.

1. Introduction

Optical agriculture has been brought to the forefront in the recent years, for providing plants with necessary light. As we know, plant growth needs four main conditions including light, atmosphere, water and nutrients, and light plays crucial roles among the four factors during all the process of plant growth.[1] According to the previous experiments of plant cultivation, the effective emission ranges are orange-red (550–700 nm) and blue (400–500 nm) bands. Plants absorb orange-red and blue light by the photosynthesis pigments of chlorophyll and phytochrome.[2,3] The latest way to promote plant growth is using LEDs to supply light in optical agricultural. Generally speaking, there are two main methods to obtain plant growth LEDs: "blue LED chip + red LED chip" and "phosphor + LED chip". For the first technology, many shortcomings such as high cost, complex control circuit, high light failure and color drift limit its further application. The main problem is that two different monochromatic semiconductor chips are used, which require different drive circuits to control the emitting light ratio of blue and red dynamically. The "phosphor + LED chip" technology can be divided into two forms for different types of chip. The first method is combined a blue-emitting InGaN chip with red emission phosphors such as $(Sr,Ca)AlSiN_3:Eu^{2+}$ [4] and $K_2TiF_6:Mn^{4+}$.[5] This technology has the advantages of simple operate and low cost. However, the inconsistency of light wane and color drift exist between blue chip and red phosphor. On the one hand, chromaticity shifts in light-emitting diode (LED) devices arise from multiple mechanisms that produce chemical changes in the materials used to construct the LED devices. The chromaticity shifts in LED devices usually start with a fast-acting component which quickly reaches its maximum value, followed by one or more slower acting component. The fast-acting and slower acting component can be modeled with a bounded exponential function and a generalized logistic function.[6] On the other hand, light wane because of the luminescence decay of phosphors in severe conditions such as high temperature, and LED device always reaches high temperature in long time work. What's more, it is difficult to guarantee the combination between the chip and phosphors, which weaken the light without effective excitation. The second approach is combined near-ultraviolet (n-UV) chips with red and blue phosphors or single-matrix red and blue dual emission phosphor, but this strategy depends more on the characteristics of phosphors and put forward higher requirements on phosphors. However, most traditional phosphors cannot match the aimed emission band, thus more accurate light sources are needed to provide the special light in the plant growth process.[7–9]

The current primary red-emitting phosphors are Eu^{2+}-doped nitrides, such as $M_2Si_5N_8:Eu^{2+}$ [10,11] and $MAlSiN_3:Eu^{2+}$ (M = Ca,

[a]*College of Science, Hunan Agricultural University, Changsha, 410128, P. R. China. E-mail: zhouzhi@hunan.edu.cn*

[b]*State Key Laboratory of Metallurgy, Central South University, Changsha, Hunan 410083, P. R. China. E-mail: xiamao2016@csu.edu.cn*

[c]*The Technology Research Centre of Hunan Optical Agricultural Engineering, Changsha, 410128, P. R. China*

† Electronic supplementary information (ESI) available. See DOI: 10.1039/c9ra00700h

‡ These authors contributed equally to this work.

This journal is © The Royal Society of Chemistry 2019

Open Access Article. Published on 21 March 2019. Downloaded on 7/13/2025 5:45:08 PM.
This article is licensed under a Creative Commons Attribution-NonCommercial 3.0 Unported Licence.

Sr, Ba).[4,12,13] They usually are synthesized in critical requirements (0.9 MPa N_2 pressure and 1800 °C), the high cost limits their utility in agricultural industry. As an alternative, Mn^{4+}-doped oxides[14–17] catch the public's attention due to its attractive luminescence properties of high-efficacy, low cost, high stability and eco-friendliness. Many strategies have been tried out to enhance the photoluminescence emission of Mn^{4+}-doped phosphors, such as matrix solid solution modification,[18–20] co-doped charge compensator[21,22] or fluxing agent,[23,24] and energy transfer from sensitizer to activator.[25–27]

Solid solution treatment is a common method in phosphor modification with many advantages such as increase lattice distortion and lattice rigidity. Some materials change phase accompanied by a large volume contraction at high temperature reaction which have damage to their luminescence properties. This phenomenon can be reduced by the addition of solid solution ions. There is no crystal transformation in the formation of solid solution, but volume effect was reduced which can enhance the resistance of phosphors to high temperature. After the formation of solid solution, there are some distortions on the lattice structure which is in a high energy activated state, and it is conducive to chemical reaction. Therefore, solid solution treatment can improve the luminescence performance and thermal stability.[28–30] There are many conditions for solid solution formation, such as similar ion radius size, alike crystal structure or chemical formula, similarity of ion electronegativity, and the same of ion value. For example, $Ca_{14}Al_{10}Zn_6O_{35}$ [31] and $Ca_{14}Ga_{10}Zn_6O_{35}$ [32] has the similar structure, Mn^{4+}-doped $Ca_{14}Al_{10}Zn_6O_{35}$ phosphors show far-red emitting, and the luminescence properties can be improved by substituting Ga^{3+} for Al^{3+} ion.[33] The similar result was found in Mn^{4+} or Ce^{3+} doped $(Y,Lu)_3(Al,Ga)_5O_{12}$ system.[22,34,35]

Another important way to enhance luminescence properties is co-doped charge compensator in same matrix. For instance, the luminescence performance of $Y_3Al_5O_{12}$:Mn^{4+} red phosphor can be enhanced by co-doping Ge^{4+}, Sc^{3+}, Ca^{2+}, Mg^{2+}, Sr^{2+}, Li^+, Na^+ ions.[21,33,36] In addition, aluminate phosphors are mainly compounded *via* high-temperature solid-state reaction in traditional production, which requires high sintering temperature. In order to reduce the reaction temperature and surface defects of the product, and increase the crystallinity of the product, fluxing agent often needs to add in the raw material such as BaF_2, NaF, NH_4Cl and H_3BO_3.[35] The third method to improve luminescence performances is to use energy transfer effect, such as $Ca_{14}Al_{10}Zn_6O_{35}$:Ti^{4+},Mn^{4+},[31] $Ca_3Al_4ZnO_{10}$:Bi^{3+},Mn^{4+},[26] Gd_2ZnTiO_6:Mn^{4+},Yb^{3+},[37] and so on.

As we know, the Mn^{4+} doped $Y_3(Al,Ga)_5O_{12}$ system show a wide range of 225–575 nm excitation spectrum. The Dy^{3+} can exhibit blue 480 nm ($^4F_{9/2}$–$^6H_{15/2}$) sharp band and orange 585 nm ($^4F_{9/2}$–$^6H_{13/2}$) luminescence performance in $Y_3(Al,Ga)_5O_{12}$ matrix for n-UV excitation.[38–41] Based on the resonance-type energy transfer theory, we assume that Dy^{3+} could improve the emission intensity of Mn^{4+} in $Y_3(Al,Ga)_5O_{12}$ matrix. Energy transfer from Dy^{3+} to Mn^{4+} has been reported in several works. Chen *et al.*[41] and Zhou *et al.*[32] verified energy transfer from Dy^{3+} to Mn^{4+} in $Ca_{14}Al_{10}Zn_6O_{35}$ and $Ca_{14}Zn_6Ga_{10}O_{35}$ phosphors respectively, which indicate that it is possible for the occurrence of similar energy transfer in $Y_3(Al,Ga)_5O_{12}$ matrix. Herein, we intend to synthesize a novel Dy^{3+} and Mn^{4+} co-doped $Y_3(Al,Ga)_5O_{12}$ phosphor which show both blue and red luminescence for plant growth LEDs.

In this study, a novel $Y_3Al_4GaO_{12}$:Mn^{4+},Dy^{3+} (YAGO:Mn^{4+},Dy^{3+}) phosphor was prepared *via* conventional solid-state method at high-temperature in air. Samples as-obtained show bright red, orange and blue light emission, which match the absorption of plant pigments in a large extent. The crystal structure, optical properties and luminescence lifetime are researched in detail. All measurements indicated that the YAGO:Mn^{4+},Dy^{3+} phosphors is promising to applicate in plant growth LEDs.

2. Experimental work

2.1 Preparation of samples and device

A series of $Y_3Al_4GaO_{12}$:Mn^{4+} (YAGO:Mn^{4+}), $Y_3Al_4GaO_{12}$:Dy^{3+} (YAGO:Dy^{3+}) and $Y_3Al_4GaO_{12}$:Mn^{4+},Dy^{3+} (YAGO:Mn^{4+},Dy^{3+}) phosphors were synthesized *via* high-temperature solid-state method. The chemical reagents were Y_2O_3 (99.999%), Ga_2O_3 (99.999%), Al_2O_3 (99.999%), Dy_2O_3 (99.999%), $Mn(NO_3)_2$ (AR), MgO (AR), H_3BO_3 (AR) and LiF (99.99%), all raw materials bought from Aladdin without further purification. Simultaneously, 5 w% H_3BO_3 (AR) and LiF acted as a flux. First of all, stoichiometric amounts of the raw material were mixed up adequately with a moderate amount of alcohol and ground thoroughly for 30 min. Then put the powder into alumina crucibles, fired at 1500 °C for heating rate at 5 °C min^{-1} in ambient atmosphere and last for 4 hours. Finally, the products were cooled to room temperature naturally and then ground for further used. The LED devices were fabricated by using the $Y_3Al_4GaO_{12}$:Mn^{4+},Dy^{3+} phosphors and 365 nm near-UV chips.

2.2 Characterization

X-ray powder diffraction (XRD) analysis was tested through a Rigaku D/SHIMADZU-6000 X-ray diffractometer with Cu-Kα radiation ($\lambda = 1.5406$ Å), operating at 40 kV and 40 mA, setting the 2θ from 10° to 80°. The photoluminescence excitation (PLE) and emission (PL) spectra were measured by F-7000 Spectrophotometer (Hitachi, Japan) equipped with a 150 W Xe lamp. For the measurement of UV-vis absorption spectra, U-3310 spectrophotometer (Hitachi, Japan) was used. The decay curves and photoluminescence quantum efficiency were measured under excitation at 366 nm *via* FLS980 fluorescence spectrometer (Edinburgh, UK) using a millisecond flash lamp. All the characterizations obtained at room temperature except the temperature-dependent PL spectra.

3. Result and discussion

3.1 Structure characterization and phase identification

The phase composition characterized by X-ray diffraction (XRD). Fig. 1(a) presents the XRD patterns of the $Y_3Al_{5-m}Ga_mO_{12}$:0.004-Mn^{4+} (m = 0–5). With the doping concentration of Ga^{3+} increased, the curve changed from $Y_3Al_5O_{12}$ (PDF#72-1315) to

Open Access Article. Published on 21 March 2019. Downloaded on 7/13/2025 5:45:08 PM.
This article is licensed under a Creative Commons Attribution-NonCommercial 3.0 Unported Licence.

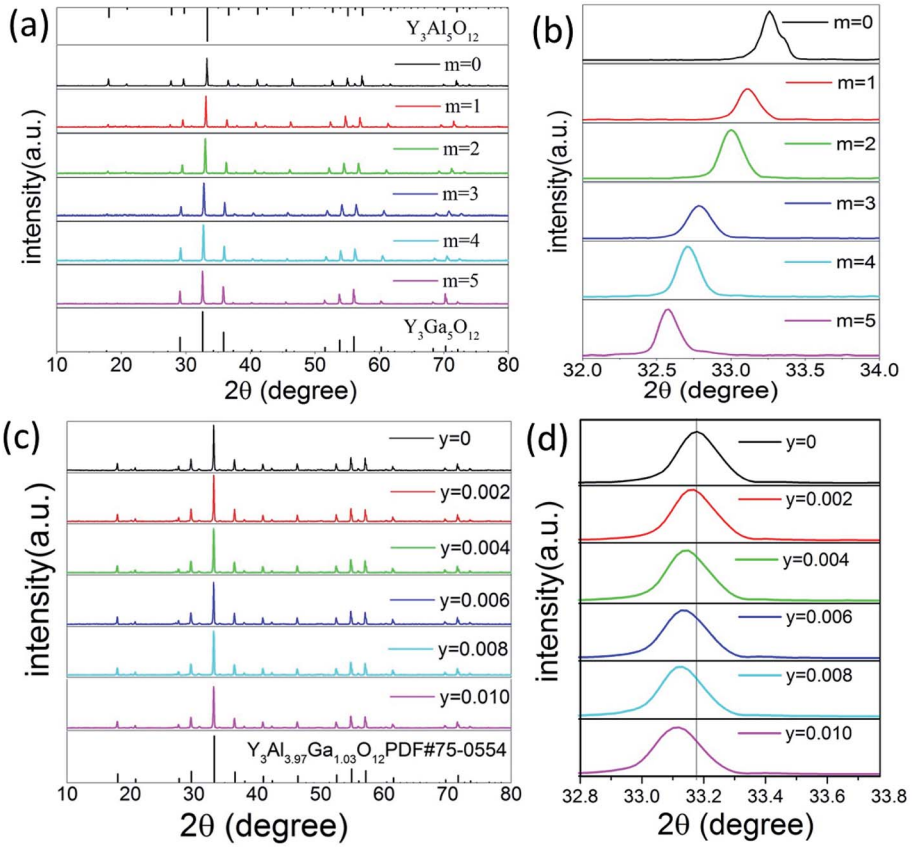

Fig. 1 (a) The XRD patterns of $Y_3Al_{5-m}Ga_mO_{12}$:0.004Mn^{4+} (m = 0–5); (b) peak position change between 32.0 and 34.0°; (c) XRD curves of $Y_3Al_4GaO_{12}$:0.004Mn^{4+},yDy^{3+} (y = 0–0.01); (d) the enlarge main peak between 32.6 and 33.8°.

$Y_3Ga_5O_{12}$ (PDF#43-0512) gradually. Fig. 1(b) shows a broad peak ranging from 32° to 34°, indicating the Al site in the matrix was replaced by Ga significantly. This substitution induced the diffraction peak of these samples shifting towards low-angel direction, because Ga^{3+} has large ionic radius (r = 0.47 Å, CN = 4; r = 0.62 Å, CN = 6) than Al^{3+} (r = 0.39 Å, CN = 4; r = 0.54 Å, CN = 6).[26] The situation was confirmed by the following analysis of PL spectra excited at different wavelengths. The XRD patterns of $Y_3Al_4GaO_{12}$:Mn^{4+},yDy^{3+} (y = 0–0.010) phosphors are shown in Fig. 1(c), which well indexed to standard card PDF#75-0554 of $Y_3Al_{3.97}Ga_{1.03}O_{12}$ phase. This result indicates $Y_3Al_4GaO_{12}$:Mn^{4+},yDy^{3+} phosphors keep its original crystal structure without significant variation. The main peak between 32.6 and 33.8° was found to be slightly offset to low-angle in Fig. 1(d), for Dy^{3+} has larger ionic radius (r = 1.03 Å, CN = 8) than Y^{3+} ion (r = 1.02 Å, CN = 8) and Mn^{4+} ion has similar ionic radius (r = 0.39 Å, CN = 4; r = 0.53 Å, CN = 6) compared to Al^{3+} ion (r = 0.39 Å, CN = 4; r = 0.53 Å, CN = 6).[42] This result is owing to the Dy^{3+} ion replaced Y^{3+} and Mn^{4+} replaced Al^{3+} ion in the [YO_8], [AlO_4] and [AlO_6] site of the matrix effectively which is similar to the literature review reported by Liudmyla M. *et al.*[43] and Chen *et al.*[32] Fig. S1(a)† presents the XRD patterns of Dy^{3+}-doped $Y_3Al_4GaO_{12}$ phosphors, and they match the standard card of $Y_3Al_{3.97}Ga_{1.03}O_{12}$ well and have the same variation tendency like Fig. 1(c).

Fig. 2 shows the unit-cell structure of $Y_3Al_{3.97}Ga_{1.03}O_{12}$ crystal (abbreviated as YAGO) and details about atomic in the cubic octahedral structure. The unit-cell is composed of three main sites. They are tetrahedral [AlO_4] octahedral [AlO_6], and dodecahedral [YO_8]. Generally, Mn^{4+} activator likes to replace the Al^{3+} in [AlO_6] site because Mn^{4+} has the similar ionic radii to Al^{3+} and octahedron are unstable compared to tetrahedron. Dy^{3+} should occupy Y^{3+} ion site in the host according to the principle of ionic radii matching,[44] which has been elucidated in the previous section. The substitution mechanism

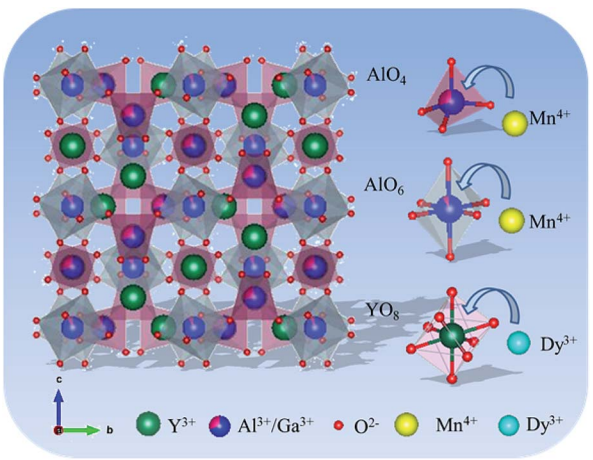

Fig. 2 Unit-cell structure of $Y_3Al_{3.97}Ga_{1.03}O_{12}$ crystal and substitution mechanism among different ion in the phosphors.

This journal is © The Royal Society of Chemistry 2019

Open Access Article. Published on 21 March 2019. Downloaded on 7/13/2025 5:45:08 PM.
This article is licensed under a Creative Commons Attribution-NonCommercial 3.0 Unported Licence.

demonstrates that Dy^{3+} replaced Y^{3+} on dodecahedral site [YO_8] and Mn^{4+} prefer to substitute Al^{3+} on octahedral [AlO_6] compared to [AlO_4] in the unit-cell structure of YAGO crystal.

3.2 Photoluminescence properties of $Y_3Al_5O_{12}$:xMn^{4+} (x = 0.002–0.010) and $Y_3Al_{5-m}Ga_mO_{12}$:0.004Mn^{4+} (m = 0–5) phosphors

Photoluminescence property is an important part to evaluate phosphors, which should be investigated in details. Fig. 3(a) and (b) show the luminescence excitation and emission spectra of $Y_3Al_5O_{12}$:0.004Mn^{4+} phosphors. When monitoring at 674 nm, there were two broad bands of each excitation spectrum that ranged from 220 to 430 nm (labeled A) and 430 to 600 nm (labeled B), and their peak located at 366 nm and 472 nm respectively. The PLE spectrum can be fitted into five Gaussian peaks, of which the 327 nm and 370 nm peaks are contributed to the $^4A_2 \rightarrow {}^4T_1$ transitions of Mn^{4+}, other peaks located at 407 nm, 469 nm and 479 nm all originated from the $^4A_2 \rightarrow {}^4T_2$ transitions of Mn^{4+}.[27] Upon excitation at 366 and 472 nm, the as-synthesized phosphors show red emission ranging from 600 to 720 nm with two peaks at 648 nm and 674 nm which can be ascribed to the spin-forbidden $^2E \rightarrow {}^4A_2$ transition of Mn^{4+}. The emission intensity came to the maximum when the concentration of Mn^{4+} was 0.004 no matter excited at 366 nm or 472 nm, as presented in the inset of Fig. 3(b). The details about the emission spectra of $Y_3Al_5O_{12}$:xMn^{4+} (x = 0.002–0.010) are shown in Fig. S3.†

Single ion doped phosphor concentration quenching model is shown in the inset of Fig. 3(a). The type of multipolar–multipolar interaction can be reflected by the formula[45] based on the Dexter's theory:

$$\frac{I}{x} = k\left[1 + \beta(x)^{\theta/3}\right]^{-1} \quad (1)$$

where k, β and θ refer to the constants for the same excitation condition, host crystal and indication of multipolar character, I and x stand for luminescence intensity and the activator concentration, respectively. Three types of dipole–dipole (d–d), dipole–quadrupole (d–q), and quadrupole–quadrupole (q–q) interactions can be speculated when θ value to 6, 8 and 10 respectively. The fitting slope is −1.4229 and the θ was calculated to be 4.2687 which is close to 6, indicating that the main quenching mechanism of YAGO:Mn^{4+} phosphor is d–d interactions.[22,29,30,32]

As shown in Fig. 3(c), it is obvious that the substitution of Ga^{3+} enhances the intensity of excitation spectra, which indicates these phosphors can be excited easily. With concentration of Ga^{3+} increasing, the intensity of photoluminescence excitation and emission spectra reached maximum when m = 1 then decreased. So we chose $Y_3Al_4GaO_{12}$ (abbreviated as YAGO) as matrix in the follow-up experiment.

3.3 Energy transfer in YAGO:Mn^{4+},Dy^{3+}phosphors

The emission of Mn^{4+} ion can be further improved *via* the addition of Dy^{3+} ion, as shown in Fig. 4(a). Two characteristic

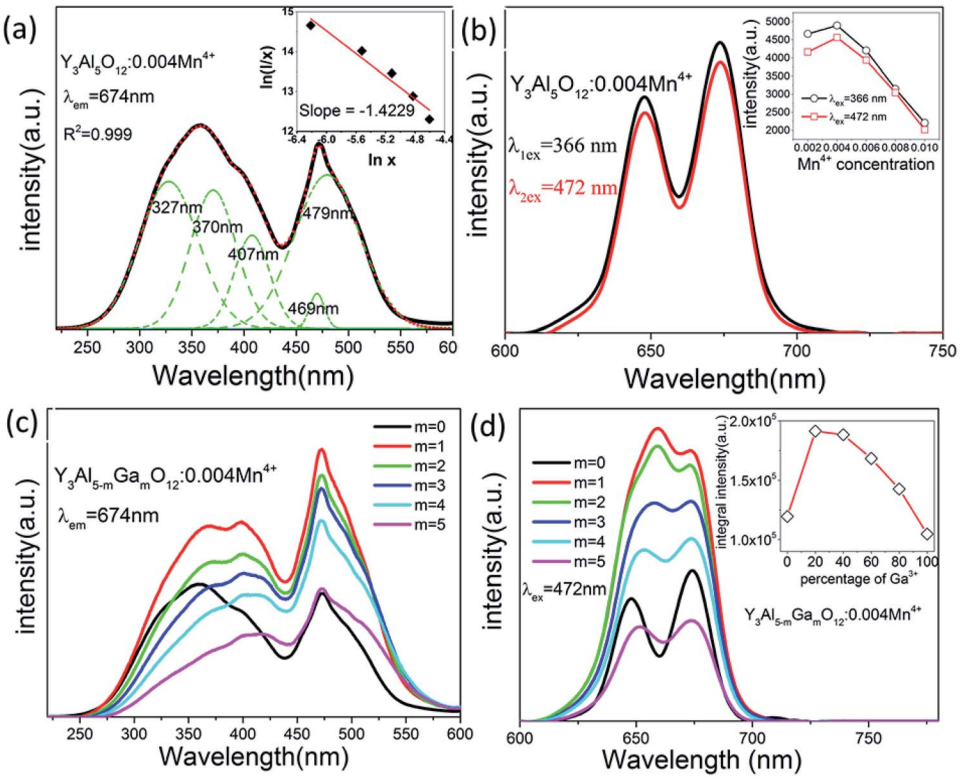

Fig. 3 (a) PLE spectrum of $Y_3Al_5O_{12}$:0.004Mn^{4+} and fitting into five Gaussian curves, inset is the dependence of log(I/x) *versus* log(x); (b) PL spectra of these samples under excitation at 366 nm and 472 nm respectively, inset is the relationship between intensity and concentration of Mn^{4+}; (c) excitation and (d) emission spectra of $Y_3Al_{5-m}Ga_mO_{12}$:0.004Mn^{4+} (m = 0–5) phosphors.

Open Access Article. Published on 21 March 2019. Downloaded on 7/13/2025 5:45:08 PM.
This article is licensed under a Creative Commons Attribution-NonCommercial 3.0 Unported Licence.

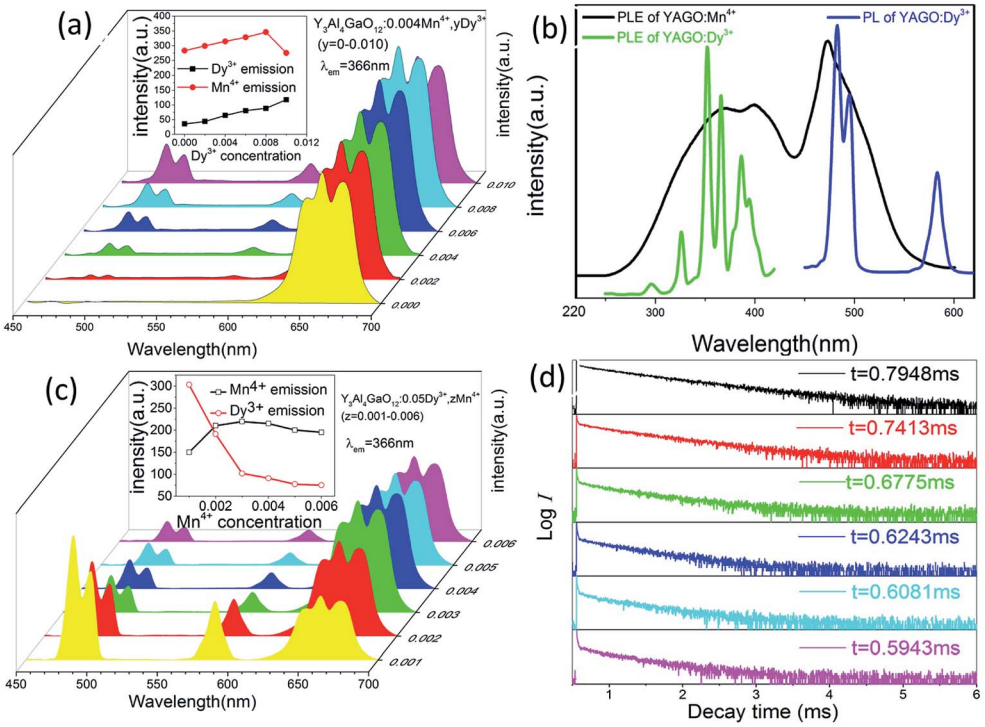

Fig. 4 (a) Photoluminescence spectra of YAGO:0.004Mn^{4+},yDy^{3+} ($y = 0$, 0.002, 0.004, 0.006, 0.008, 0.010), inset is the change of emission intensity of two ions with different Dy^{3+} concentration; (b) the excitation spectrum of YAGO:Mn^{4+} (black line), the PLE (green line) and PL spectra (blue line) of YAGO:Dy^{3+}; (c) PL spectra of YAGO:0.05Dy^{3+},zMn^{4+} ($z = 0.001$–0.006) under excitation at 366 nm, inset is the change of emission intensity of two ions with different Mn^{4+} concentration; (d) decay curves of YAGO:0.05Dy^{3+},zMn^{4+} ($z = 0.001$–0.006) monitored at 483 nm under excitation at 366 nm.

emission bands can be detected at 462–490 nm and 554–607 nm in YAGO:Mn^{4+},Dy^{3+} phosphor under excitation at 366 nm, which corresponding to $^4F_{9/2} \rightarrow {}^6H_{15/2}$ and $^4F_{9/2} \rightarrow {}^6H_{13/2}$ transitions in the 4f levels of Dy^{3+} ions, respectively.[46] And red emission ranging from 600 to 720 nm should be ascribed to the $^2E \rightarrow {}^4A_2$ transition of Mn^{4+}. What's more, Fig. S2(a) and (b)† show the photoluminescence excitation and emission spectra of YAGO:Dy^{3+}, the optimal Dy^{3+} doping concentration is 0.05. The excitation peaks located at 326.5, 352.5, 366.5 and 387.0 nm attribute to the intrinsic f–f transitions of Dy^{3+} from the ground state $^6H_{15/2}$ to the excited state $^4L1_{9/2}$, $^6P_{7/2}$, $^6P_{5/2}$ and $^4I_{13/2}$, respectively.[46]

Fig. 4(b) presents a large overlapping part between the PLE spectrum of YAGO:Mn^{4+} and the PL spectrum of YAGO:Dy^{3+}. It is one of the indispensable factors for effective energy transfer. Therefore, it is possible for the occurrence of energy transfer from Dy^{3+} to Mn^{4+} ions in YAGO matrix. In order to confirm the energy transfer further, the content of Dy^{3+} ion was fixed at 0.05 and the concentration of Mn^{4+} was increased from 0.001 to 0.006. According to Fig. 4(c), with the concentration of Mn^{4+} increasing, the emission of Dy^{3+} decreased gradually while the emission of Mn^{4+} increased until Mn^{4+} concentration exceed 0.003 and then decreased due to the concentration quenching effect. Such experimental results are consistent with the prediction that there is energy transfer from Dy^{3+} to Mn^{4+} in YAGO host.

As mentioned in Fig. 4(c), the emission intensity of Mn^{4+} decrease when the content of Mn^{4+} exceeds the critical concentration because of the concentration quenching phenomenon which is related to energy transfer. In generally, the critical distance (R_c) is a key parameter to evaluate the performance of sensitizer and activator, which is usually calculated by the following formula:[47,48]

$$R_c = 2\left[\frac{3V}{4\pi x_c N}\right]^{1/3} \quad (2)$$

where V, N and x_c refer to the volume of the unit cell, the critical concentration of Mn^{4+} and the number of lattice sites in the unit cell that can be occupied by activators, respectively. Herein, V is 1754.05 Å, x_c is 0.0025 and N is 8 for YAGO:Mn^{4+},Dy^{3+} phosphors, then the critical distance R_c was calculated to be 55.13 Å.

The PL decay curves were investigated to calculate the lifetime and then to verify the energy transfer from Dy^{3+} to Mn^{4+}. Monitor at 483 nm for YAGO:Mn^{4+},Dy^{3+} phosphors under the excitation of 366 nm, the decay curves are illustrated in Fig. 4(d). These data fitted a typical single-exponential function well:[25]

$$I = I_0 \times \exp\left(\frac{-t}{\tau}\right) \quad (3)$$

where t refer to the time and I is the luminescence intensity at that moment, I_0 and τ stand for the initial emission intensity at time 0 and the luminescence lifetime, respectively. For YAGO:0.05Dy^{3+},zMn^{4+} ($z = 0.001$–0.006) phosphors, the lifetime of Dy^{3+} decreased distinctly with the content of Mn^{4+} increasing. They were 0.795, 0.741, 0.678, 0.624, 0.608 and 0.594 ms when

 This journal is © The Royal Society of Chemistry 2019

Open Access Article. Published on 21 March 2019. Downloaded on 7/13/2025 5:45:08 PM.
This article is licensed under a Creative Commons Attribution-NonCommercial 3.0 Unported Licence.

the content of Mn^{4+} changed from 0.001 to 0.006, respectively. This result prove that energy transfer from Dy^{3+} to Mn^{4+} exist in these samples, similar conclusion in $Ca_{14}(Al,Ga)_{10}Zn_6O_{35}$ matrix was reported by Zhou *et al.*[31]

Fig. 5(a) presents the UV-vis absorption spectra of YAGO, YAGO:Mn^{4+}, YAGO:Dy^{3+} and YAGO:Mn^{4+},Dy^{3+}. Two characteristic absorption bands were found in all four samples that name Band A (220–260 nm) and Band B (260 to 430 nm). Band C (430–550 nm) existed only in Mn^{4+}-doped phosphor, which should be attributed to the $^4A_2 \rightarrow {}^4T_1$ transition of Mn^{4+}. The absorption intensity enhanced by adding Dy^{3+} ion, and further enhanced by co-doping Mn^{4+} and Dy^{3+} ions.

To understand the effect of the addition of Mn^{4+} and Dy^{3+} ions on YAGO matrix, the band gap of four materials were researched, which can be calculated by the following equation according to the UV-vis absorption plots:[49]

$$(\alpha h\nu)^2 = A(h\nu - E_g) \quad (4)$$

where α, h, ν and A are the absorption coefficient, the Planck constant, the frequency and constant; and E_g is the band gap energy. According to the equation and absorption dates, the relationship between the plot of $(\alpha h\nu)^2$ and $h\nu$ based on the direct gap are presented in Fig. 5(b). The value of the band gap E_g for YAGO, YAGO:Mn^{4+}, YAGO:Dy^{3+} and YAGO:Mn^{4+},Dy^{3+} were calculated to be 4.12 eV, 4.10 eV, 3.15 eV and 3.06 eV, respectively. There is a great change of band-gap after Mn^{4+}-doping (from 4.12 to 3.15 eV), which can be explained by the electronegativity of ions. In the one hand, it requires less energy for electrons to get rid of the limiting valance bonds when Mn^{4+} ion replace Al^{3+} and Ga^{3+} ion because Mn^{4+} ion has lower electronegativity than Al^{3+} and Ga^{3+} ion, which resulting in a reduce in energy band gap.[26] Meanwhile, Dy^{3+} dopant could also reduce the band gap slightly for its small electronegativity. In the other hand, the intimate addiction of E_g on Mn^{4+} ions concentration indicates that the Mn^{4+} orbitals are probably involved in the conduction band besides of the band gap of YAGO.

According to Reisfeld's approximation and Dexter's energy transfer formula of multipolar interaction, the equation can evaluate interaction mechanism:[50,51]

$$\frac{\eta_0}{\eta} = C^{n/3} \quad (5)$$

herein, C is the sum of the concentration of Mn^{4+} and Dy^{3+}, η and η_0 stand for the luminescence quantum efficiency of Dy^{3+} in the presence and absence of Mn^{4+}, respectively. The η_0/η is usually calculated through the ratio of initial luminescence intensity of YAGO:Dy^{3+} and YAGO:Dy^{3+},Mn^{4+}, and the equation can be written as $I_{so}/I_s \propto C^{n/3}$. Based on the formula, three types of interaction named dipole–dipole (d–d), dipole–quadrupole (d–p) and quadrupole–quadrupole (p–p) can be expected while $n = 6$, 8 and 10 respectively. Fig. 6 presents the relationship between I_{so}/I_s and C. When $n = 6$, linear fitting come to optimum with $R^2 = 0.998$, implying that it is dipole–dipole interaction mechanism for the energy transfer from Dy^{3+} to Mn^{4+} in YAGO phosphor.

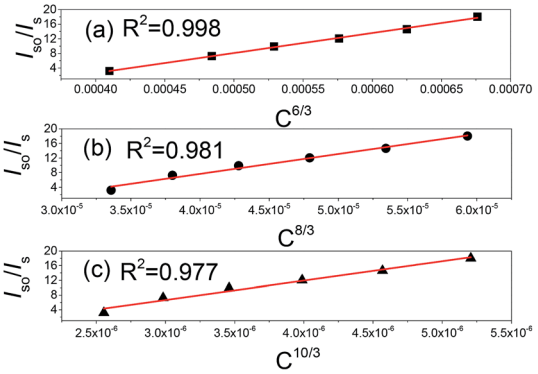

Fig. 6 Linear relationship between I_{so}/I_s and $C^{n/3}$ (a) $n = 6$, (b) $n = 8$, (c) $n = 10$.

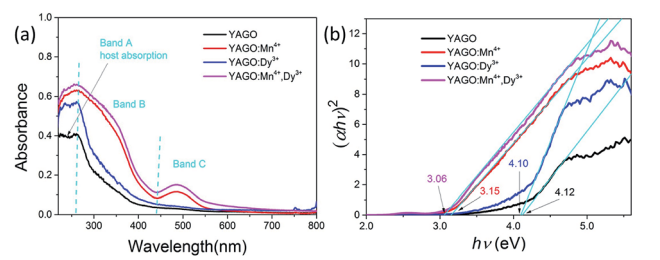

Fig. 5 (a) Comparison the UV-vis absorption spectra of YAGO phosphors with different dopants; (b) the plot of $(\alpha h\nu)^2$ *versus* $h\nu$ based on the direct gap of different samples.

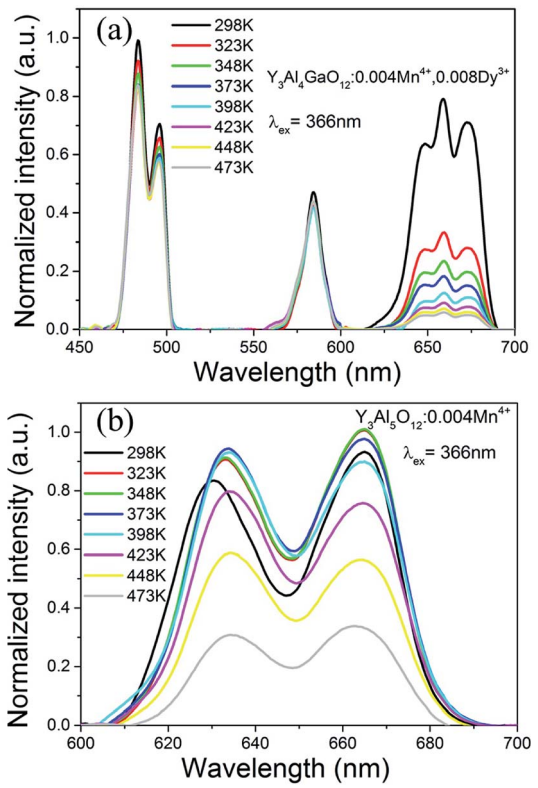

Fig. 7 Temperature-dependent emission spectra of (a) $Y_3Al_4GaO_{12}$:Mn^{4+},Dy^{3+} and (b) $Y_3Al_5O_{12}$:Mn^{4+} from 298 K to 473 K under excitation at 366 nm.

Open Access Article. Published on 21 March 2019. Downloaded on 7/13/2025 5:45:08 PM.
This article is licensed under a Creative Commons Attribution-NonCommercial 3.0 Unported Licence.

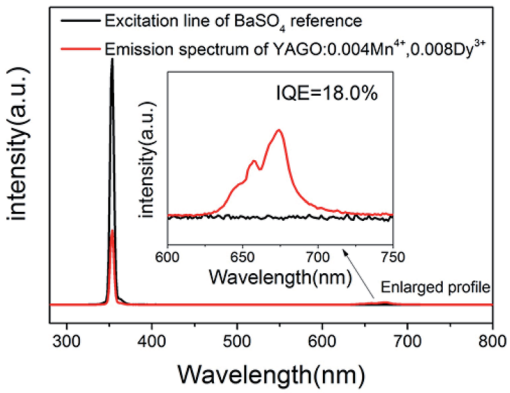

Fig. 8 Excitation line of $BaSO_4$ and the PL spectrum of $Y_3Al_4GaO_{12}$:0.004Mn^{4+},0.008Dy^{3+} phosphor collected using an integrating sphere.

We tested the temperature-dependent emission spectra of $Y_3Al_4GaO_{12}$:0.004Mn^{4+},0.008Dy^{3+} and $Y_3Al_5O_{12}$:0.004Mn^{4+} from 298 K to 473 K in details, as shown in Fig. 7. The integral intensity of the YAGO:Mn^{4+},Dy^{3+} sample kept 59.61% when the temperature came to 423 K while YAG:Mn^{4+} maintained 90.10%. Though it seems decreased in the value of thermal stability, other effective emission bands for plant growth lighting were induced and keep its thermal stability well. In addition, it is possible that its thermal stability can be improved through a series of modifications in the future.

The quantum yield of $Y_3Al_4GaO_{12}$:0.004Mn^{4+},0.008Dy^{3+} phosphor was measured under 366 nm excitation which as shown in Fig. 8, the value of IQE was calculated to be 18.0% through the following equation:[52]

$$\eta = \frac{\int L_S}{\int E_R - \int E_S} \quad (6)$$

where η and L_S are IQE and the emission spectrum of the sample, E_S and E_R are the spectra of excitation light with sample and only with $BaSO_4$ reference, respectively. This IQE is at a low level likes $SrLaScO_4$:Mn^{4+} (IQE: 12.2%)[53] and $Ca_{14}Al_{10}Zn_6O_{35}$:Mn^{4+} (IQE: 19.4%)[54] which have been reported, and the property would be increased further.

For clearly describing the energy change in YAGO:Mn^{4+},Dy^{3+} phosphor, the excitation, emission and energy transfer processes of the sample were shown in Fig. 9. Dy^{3+} ions were excited from $^6H_{15/2}$ energy level to high excited state level such as $^6P_{7/2}$, $^4I_{13/2}$, $^4F_{9/2}$ or even the conduction under irradiation of the n-UV light, then relaxed to $^6H_{13/2}$ and $^6H_{15/2}$ from $^4F_{9/2}$ with blue and orange emission. Meanwhile, Mn^{4+} ion can be excited to $^4T_1$, $^4T_2$ level and conduction band from $^4A_2$ under n-UV radiation, the excited Mn^{4+} dropped to the ^2E energy level then relaxed to $^4A_2$ with red light emission. In this process, the energy transfer occurs from excited state level $^4F_{9/2}$ of Dy^{3+} ions to the excited state level $^4T_2$ of Mn^{4+} ions, then relaxed to the lowest excited state level ^2E of Mn^{4+} ions through non-radiative relaxation, finally came back to the ground state in the form of red emission.

3.4 LED device fabricated with YAGO:Mn^{4+},Dy^{3+} and its electro-luminescent property

In order to investigate the application of the synthetic YAGO:Mn^{4+},Dy^{3+} in indoor plant growth, LED devices were fabricated with YAGO:Mn^{4+},Dy^{3+} phosphor and 365 nm near-UV chip. As shown in Fig. 10(a), the phosphor powder was white in daylight and presented purplish red under the ultraviolet lamp; it appeared milky white in the LED device and sent bright purplish red emission under constant current of 20 mA. The electroluminescence spectrum was mainly consisted of red, blue and little orange emission from YAGO:Mn^{4+},Dy^{3+} phosphor and near ultraviolet emission from the chip, which

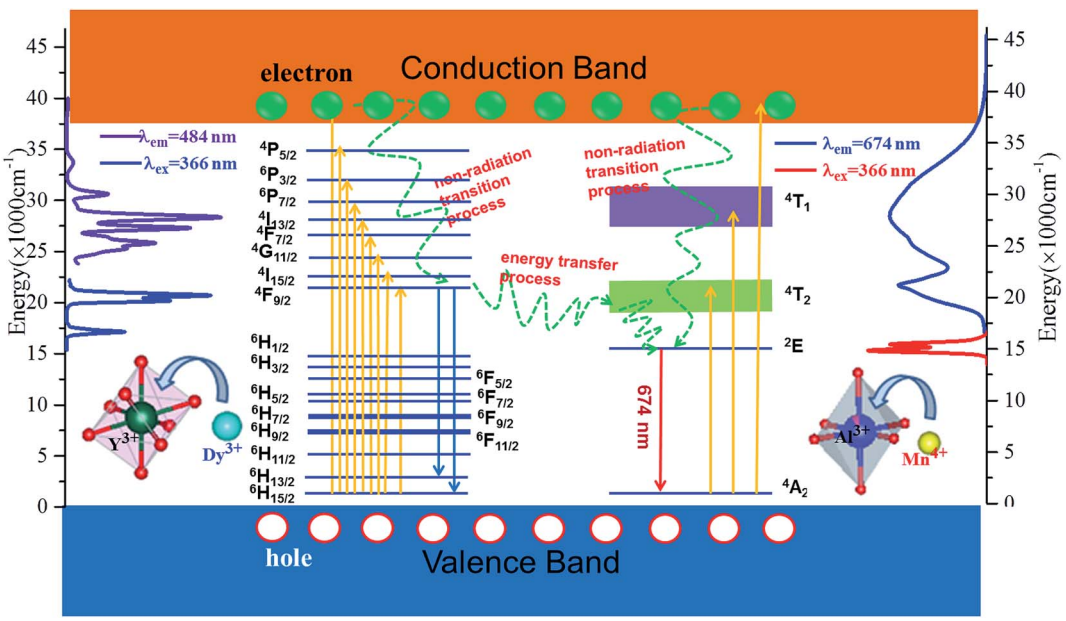

Fig. 9 Energy level, electron transitions and energy transfer schematic diagram of Dy^{3+} and Mn^{4+} in YAGO matrix.

This journal is © The Royal Society of Chemistry 2019

Open Access Article. Published on 21 March 2019. Downloaded on 7/13/2025 5:45:08 PM.
This article is licensed under a Creative Commons Attribution-NonCommercial 3.0 Unported Licence.

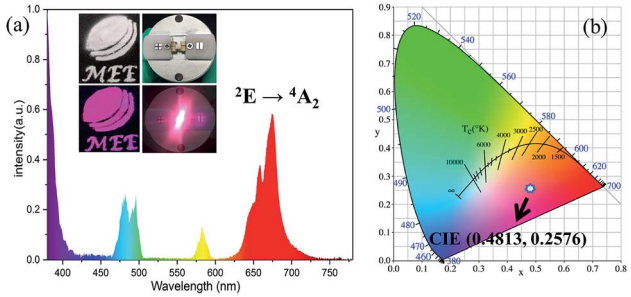

Fig. 10 (a) Electroluminescence spectrum of the as-fabricated LED device by using YAGO:0.004Mn^{4+},0.008Dy^{3+} phosphors and a 365 nm near-UV LED chip under a current of constant current of 20 mA. Insets are the images of LED device and phosphor powder in daylight and under a 365 nm UV lamp. (b) CIE chromaticity coordinates of the sample.

consistent with luminescence spectrum of the sample. Fig. 10(b) shows the resultant CIE coordinate value of this LED device was (0.4813, 0.2576). Other CIE coordinate values of devices that combined with different concentration of Mn^{4+} and Dy^{3+} co-doped YAGO phosphor are exhibited in Fig. S4,† they changed from purplish red to white light gradually with the increasing content of Dy^{3+}. The result suggests that the novel YAGO Mn^{4+},Dy^{3+} phosphor have potential application in plant growth lighting and white LED lighting for their unique optical property.

4. Conclusions

To sum up, Mn^{4+} and Dy^{3+} co-doped YAGO phosphors were successfully synthesized *via* conventional high-temperature solid-state method. These phosphors are derived from the crystal structure of $Y_3Al_5O_{12}$ and changed to $Y_3Al_4GaO_{12}$ host, activators Mn^{4+} replacing Al^{3+} site while Dy^{3+} occupying Y^{3+} site in the matrix. The $Y_3Al_4GaO_{12}$:Mn^{4+},Dy^{3+} phosphors show blue, orange and red emission located at 462–490 nm, 554–607 nm and 625–700 nm respectively, which match the absorption spectrum of plant pigment well. And, these three emission bands can be ascribed to the $^4F_{9/2} \rightarrow {}^6H_{15/2}$ and $^4F_{9/2} \rightarrow {}^6H_{13/2}$ transition of Dy^{3+} and the $^2E \rightarrow {}^4A_2$ transition of Mn^{4+}, respectively. When the doping concentration of Mn^{4+} was 0.4% and Dy^{3+} was 0.8%, optimal property of these phosphors was obtained. There are many evidences for energy transfer from Dy^{3+} to Mn^{4+} in the as-obtained $Y_3Al_4GaO_{12}$:Mn^{4+},Dy^{3+} phosphors. Moreover, LED devices made from the phosphor have good properties. It is indicate that the as-obtained phosphors have potential applications both in optical agriculture and white LED lighting.

Conflicts of interest

There are no conflicts to declare.

Acknowledgements

The authors would like to gratefully acknowledge funds from National Natural Science Foundation of China (Grant No. 21706060, 51703061), Natural Sciences Foundation of Hunan Province, China (Grant No. 2017JJ3103), Scientific Research Foundation of Hunan Provincial Education Department (Grant No. 17B118) and Hunan Provincial Engineering Technology Research Center for Optical Agriculture (Grant No. 2018TP2003).

Notes and references

1 M. Kula, M. Rys, K. Mozdzen and A. Skoczowski, *Eng. Life Sci.*, 2014, **14**, 57–67.
2 T. Nakajima and T. Tsuchiya, *ACS Appl. Mater. Interfaces*, 2015, **7**, 21398–21407.
3 L. Poulet, G. D. Massa, R. C. Morrowc, C. M. Bourget, R. M. Wheeler and C. A. Mitchell, *Life Sci. Space Res.*, 2014, **2**, 43–53.
4 X. Piao, K. Machida, T. Horikawa, H. Hanzawa, Y. Shimomura and N. Kijima, *Chem. Mater.*, 2007, **19**, 4592–4599.
5 M. Fang, C. Hsu, Ch. Su, W. Liu, Y. Wang and R. S. Liu, *ACS Appl. Mater. Interfaces*, 2018, **10**, 29233–29237.
6 J. Davis, K. Mills, G. Bobashev, K. Rountree, M. Lamvik, R. Yaga and C. Johnson, *Microelectron. Reliab.*, 2018, **84**, 149–156.
7 C. W. Yeh, W. T. Chen, R. S. Liu, S. F. Hu, H. S. Sheu, J. M. Chen and H. T. Hintzen, *J. Am. Chem. Soc.*, 2012, **134**, 14108–14117.
8 K. T. Bicanic, X. Li, R. P. Sabatini, N. Hossain, C. Wang, F. Fan, H. Liang, S. Hoogland and E. H. Sargent, *ACS Photonics*, 2016, **3**, 2243–2248.
9 Z. Zhou, N. Zhou, M. Xia, Y. Meiso and H. T. (Bert) Hintzen, *J. Mater. Chem. C*, 2016, **4**, 9143–9161.
10 Y. Q. Li, J. E. J. van Steen, J. W. H. van Krevel, G. Botty, A. C. A. Delsing, F. J. DiSalvo, G. de With and H. T. Hintzen, *J. Alloys Compd.*, 2006, **417**, 273–279.
11 Y. Q. Li, G. de With and H. T. Hintzen, *J. Solid State Chem.*, 2008, **181**, 515–524.
12 J. Li, T. Watanabe, H. i. Wada, T. Setoyama and M. Yoshimura, *Chem. Mater.*, 2007, **19**, 3592–3594.
13 Y. Tsai, C. Chiang, W. Zhou, J. F. Lee, H. Sheu and R. S. Liu, *J. Am. Chem. Soc.*, 2015, **137**, 8936–8939.
14 R. Cao, T. Chen, Y. Ren, T. Chen, H. Ao, W. Li and G. Zheng, *J. Alloys Compd.*, 2019, **780**, 749–755.
15 Y. Ren, R. cao, T. Chen, L. Su, X. Cheng, T. Chen, S. Guo and X. Yu, *J. Lumin.*, 2019, **209**, 1–7.
16 R. Cao, X. Liu, K. Bai, T. Chen, S. Guo, Z. Hu, F. Xiao and Z. Luo, *J. Lumin.*, 2018, **197**, 169–174.
17 K. Li, D. Mare and R. V. Deun, *Dalton Trans.*, 2019, **48**, 3187–3192.
18 K. Sankarasubramanian, B. Devakumar, G. Annadurai, L. Sun, Y. Zeng and X. Huang, *RSC Adv.*, 2018, **8**, 30223–30229.
19 Q. Sun, S. Wang, B. Li, H. Guo and X. Huang, *J. Lumin.*, 2018, **203**, 317–375.
20 Q. Sun, S. Wang, B. Devakumar, B. Li, L. Sun, J. Liang and X. Huang, *RSC Adv.*, 2018, **8**, 28538–28545.

Open Access Article. Published on 21 March 2019. Downloaded on 7/13/2025 5:45:08 PM.
This article is licensed under a Creative Commons Attribution-NonCommercial 3.0 Unported Licence.

21 D. Chen, Y. Zhou, W. Xu, J. Zhong, Z. Ji and W. Xiang, *J. Mater. Chem. C*, 2016, **4**, 1704–1712.
22 L. Sun, B. Devakumar, J. Liang, B. Li, S. Wang, Q. Sun, H. Guo and X. Huang, *RSC Adv.*, 2018, **8**, 31835–31842.
23 Y. Yu, H. Wang, L. Li, Y. Chen and R. Zeng, *Ceram. Int.*, 2014, **40**, 14171–14175.
24 S. Xu, L. Sun, Y. Zhang, H. Ju, S. Zhao, D. Deng, H. Wang and B. Wang, *J. Rare Earths*, 2009, **27**, 327–329.
25 Z. Zhou, M. Xia, Y. Zhong, Sh. Gai, S. Huang, Y. Tian, X. Lu and N. Zhou, *J. Mater. Chem. C*, 2017, **5**, 8201–8210.
26 Z. Zhou, Y. Zhong, M. Xia, N. Zhou, B. Lei, J. Wang and F. Wu, *J. Mater. Chem. C*, 2018, **6**, 8914–8922.
27 J. Zhou, Q. Liua and Z. Xia, *J. Mater. Chem. C*, 2018, **6**, 4371–4383.
28 X. Ji, J. Zhang, Y. Li, S. Liao, X. Zhang, Z. Yang, Z. Wang, Z. Qiu, W. Zhou, L. Yu and S. Lian, *Chem. Mater.*, 2018, **30**, 5137–5147.
29 K. Li, D. Zhu and R. V. Deun, *Dyes Pigm.*, 2017, **142**, 69–76.
30 K. Li, D. Zhu and R. V. Deun, *Dalton Trans.*, 2018, **47**, 2501–2505.
31 Z. Zhou, Y. Li, M. Xia, Y. Zhong, N. Zhou and H. T. (Bert) Hintzenc, *Dalton Trans.*, 2018, **47**, 13713–13721.
32 Y. Zhou, W. Zhao, J. Chen and Z. Liao, *RSC Adv.*, 2017, **7**, 17244–17253.
33 D. Chen, Y. Zhou, W. Xu, J. Zhong, Z. Ji and W. Xiang, *J. Mater. Chem. C*, 2016, **4**, 9044–9051.
34 Y. Zhou, W. Zhao, C. Lu and Z. Liao, *Prog. Nat. Sci.: Mater. Int.*, 2018, **28**, 301–307.
35 W. Xu, D. Chen, S. Yuan, Y. Zhou and S. Li, *Chem. Eng. J.*, 2017, **317**, 854–861.
36 J. Long, Y. Wang, R. Ma, C. Ma, X. Yuan, Z. Wen, M. Du and Y. Cao, *Inorg. Chem.*, 2017, **56**, 3269–3275.
37 J. Xiang, J. Chen, N. Zhang, H. Yao and C. Guo, *Dyes Pigm.*, 2018, **154**, 257–262.
38 L. M. Chepygaa, A. Osvet, C. J. Brabecb and M. Batentschuk, *J. Lumin.*, 2017, **182**, 200–207.
39 J. F. C. Carreira, N. B. Sedrine, T. Monteiro and L. Rino, *J. Lumin.*, 2017, **183**, 251–258.
40 J. Y. Chong, Y. Zhang, B. K. Wagner and Z. Kang, *J. Alloys Compd.*, 2013, **581**, 484–487.
41 J. Chen, W. Zhao, N. Wang, Y. Meng, S. Yi, J. He and X. Zhang, *J. Mater. Sci.*, 2016, **51**, 4201–4212.
42 R. D. Shannon, *Acta Crystallogr.*, 1976, **32**, 751–767.
43 E. Hertle, L. Chepyga, M. Batentschuk and L. Zigan, *J. Lumin.*, 2017, **188**, 582–588.
44 K. Li, H. Lian and R. V. Deun, *J. Lumin.*, 2018, **198**, 155–162.
45 D. L. Dexter, *J. Chem. Phys.*, 1953, **21**, 836–850.
46 Q. Liu, Y. Liu, Z. Yang, Y. Han, X. Li and G. Fu, *J. Alloys Compd.*, 2012, **515**, 16–19.
47 G. Blasse, *Phys. Lett. A*, 1968, **28**, 444–445.
48 X. Huang, B. Li and H. Guo, *J. Alloys Compd.*, 2017, **695**, 2773–2780.
49 L. Wu, Y. Zhang, M. Gui, P. Lu, L. Zhao, S. Tian, Y. Kong and J. Xu, *J. Mater. Chem.*, 2012, **22**, 6463–6470.
50 D. L. Dexter and J. H. Schulman, *J. Chem. Phys.*, 1954, **22**, 1063–1070.
51 Y. F. Nicolau and J. C. Menard, *J. Cryst. Growth*, 1988, **92**, 128–142.
52 X. Ding, G. Zhu, W. Geng, Q. Wang and Y. Wang, *Inorg. Chem.*, 2015, **55**, 154–162.
53 U. B. Humayoun, S. N. Tiruneh and D. H. Yoon, *Dyes Pigm.*, 2018, **152**, 127–130.
54 L. Li, Y. Pan, Z. Chen, S. Huang and M. Wu, *RSC Adv.*, 2017, **7**, 14868–14875.

This journal is © The Royal Society of Chemistry 2019